Ionic Thruster Diagnostics by Means of PIV and LPT

Dominic Poeppe*, Tomos Rich, Jochen Kriegseis

Institute of Fluid Mechanics (ISTM), Karlsruhe Institute of Technology, Germany

*Corresponding author: poeppe@kit.edu

Keywords: ionic propulsion, electroaerodynamic propulsion, force from velocity, planar particle image velocimetry (PIV), Lagrangian particle tracking (LPT), 4-pulse Shake-the-Box (STB).

ABSTRACT

Particle image velocimetry (PIV) and Lagrangian particle tracking (LPT) by means of shake-the-box (STB) evaluation are presented as complementary experimental techniques for the diagnosis of the momentum-transfer characteristics of ionic thrusters. PIV evaluation enables high-resolution and near-wall velocity fields over a large area for a single wire-to-airfoil electrode pair and delivers accurate thrust readings via the integral momentum equation when fluctuations in the velocity field are accounted for. This is contrast with a differential approach based on the Navier-Stokes equation and leveraging the explicit capability of LPT to measure material acceleration. Wire-to-airfoil and wire-to-grid thruster configurations are tested, showcasing limitations due to optical access and glare, particularly with wire-to-airfoil configurations. The LPT velocity fields agree with the PIV fields, serving as cross-validation. In novel findings, the LPT acceleration fields of the wire-to-grid thruster configuration show channel-like acceleration regions in the drift zone and a major impact of pressure gradients on the thrust generation.

1. Introduction

Ionic wind, also known as electroaerodynamic (EAD) propulsion, has garnered significant interest in recent years due to its potential for providing efficient, zero-emissions, and low-maintenance thrust systems [1, 2]. Consequently, EAD thrusters enjoy increasing attention for aeronautical propulsion and have been proven to be a candidate electrical propulsion system [3, 4]. The thrusters are typically comprised of wires as high-voltage DC emitters and either cylinders [5, 6] or aerodynamic profiles [7, 8] as grounded collectors to maintain the ionic wind. More recently, grid collectors have been shown to greatly increase thrust density [9]. In order to further improve the overall performance of those thrusters, recent research efforts address the identification, characterization and optimization of involved phenomena – mainly on the basis of electrical, chemical, optical and fluid-mechanical quantities and their respective interplay.

The operating principle of positive corona discharge EAD thrusters is based on imparting momentum onto neutral air molecules by collisions with ions, which are in turn accelerated by the

electric drift field in the so-called drift region between two electrodes. The sharply curved emitting electrode, referred to as emitter, usually has positive potential, while the collecting electrode, referred to as collector, is grounded. The electric field strength reaches its peak in the immediate vicinity around the emitter, leading to an ionization cascade. The upper limit of thrust T can be approximated analytically when neglecting space charge effects as $T = Id/\mu$, where I is the discharge current, d is the gap distance between the emitter and collector electrodes, and μ is the ion mobility [3, 10]. The thrust of practical single thrusters is furthermore, but not exhaustively, a function of emitter and collector shape influencing the electric field shape and body drag, air speed, environmental quantities, and three-dimensional effects due to finite span.

Key metrics of EAD thrusters include absolute thrust (or thrust density) and efficiency (thrust per power), which exhibit an inverse relationship [10]. Optimizing the Pareto front of these two quantities is thus key to future high-performance thruster design.

The objective of this study is a comparative diagnostics framework for momentum transfer of EAD thrusters using two distinct approaches. First is an Eulerian investigation using particle image velocimetry (PIV). The aim of this is to attain high spatially resolved velocity fields and investigate the feasibility of calculating the thrust produced from velocity data, where major emphasis is placed on integral methods for thrust evaluation. This is expanded and complemented by Lagrangian particle tracking (LPT) velocimetry, which instead leverages the differential form of the momentum equation to calculate the volumetric distribution of the ionic force between the electrodes of the thruster on the grounds of directly measured material acceleration of the fluid.

section 2 introduces the experimental setup of both the PIV and LPT investigations. This is followed by the discussion of the PIV data and an evaluation of the momentum-balance based thrust estimation in section 3 and section 4, respectively. section 5 introduces the theory behind material acceleration from Lagrangian data and section 6 discusses the resulting experimental findings.

2. Experimental Procedure

The diagnostics framework to analyze the fluid-mechanical thruster performance is comprised of two sets of experiments – Particle image velocimetry (PIV) and Lagrangian particle tracking (LPT) by means of shake-the-box (STB). While PIV is considered to cover a large field of view and accordingly evaluate the overall flow topology in proximity of the thrusters, the STB results will take immediate advantage of the Lagrangian character of the recorded data in terms of material accelerations for a force-field evaluation.

2.1. Particle Image Velocimetry

The experimental setup for the PIV investigation consists of a single wire-to-airfoil pair, which can be seen in Figure 1. While arrays of emitter-collector pairs have been shown to be superior [5, 8, 10–15] and are used for the STB experiments, this deliberate choice is made in order to facilitate optimum optical access and to build an undisturbed baseline measure of a single pair as reference for future array comparisons.

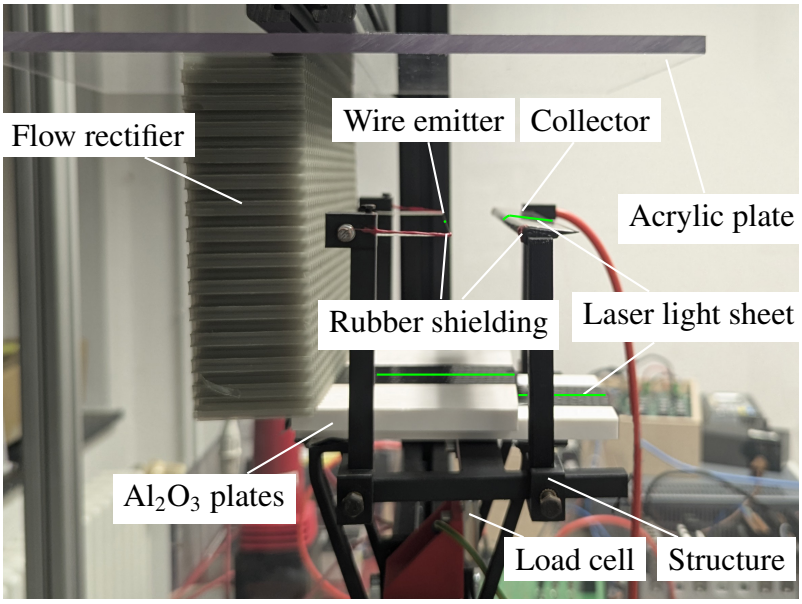


Figure 1. Experimental setup of the thruster used with all major components labeled. Perspective similar to PIV camera.

The geometric and operating parameters for the PIV study are summarized as follows:

- Span $b = 200\,\text{mm}$
- Inter-electrode gap distance $d = 30\,\text{mm}$
- Wire emitter with diameter of $D_e = 100\,\mu\text{m}$
- Droplet airfoil collector
  - Thickness to chord ratio $t/c = 0.24$
  - Thickness $t = 6\,\text{mm}$
- operating voltage 15 kV to 30 kV

The layout of the spatial arrangement and the corresponding dimensions are furthermore sketched in Figure 2.

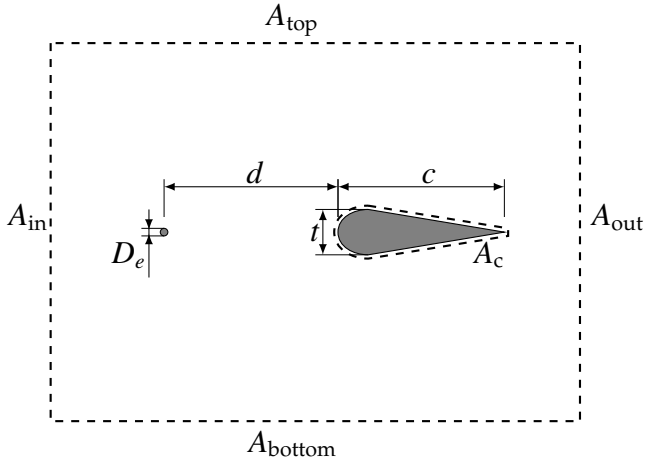


Figure 2. Sketch of geometric parameters of the wire-to-airfoil thruster used in this paper (Not to scale). Surrounding the thruster is the control volume definition used in the integral momentum balance in section 3.

The emitter wire is a constantan alloy, while the collector is a stereolithography 3D-printed structure, coated with aluminum and polished to reduce undesirable diffuse laser light reflection. The span-wise edges of the emitter and collector are coated in an insulating rubber to eliminate edge effects such as reverse corona discharge and arc discharge. Emitter and collector are affixed to an insulating plastic structure, which is mounted to the load cell. To reduce the strength of the parasitic electric field between the emitter and the grounded load-cell, Al_2O_3 plates are installed due to their high permittivity (see Figure 2. The operating voltage is provided by a GBS Elektronik Minipuls 6 in combination with a high-voltage multiplier cascade and regulated using a PID controller.

In order to reduce the effects of fluctuating inflow conditions arising from potential large-scale motions within the enclosure, a honeycomb structure acts as a flow rectifier for the data presented in section 3. It is positioned 60 mm upstream of the emitter. Since this rectifier introduces aerodynamic drag and would thus need to be accounted for in the momentum balance calculation of section 4, it is instead omitted for the velocity-information-based thrust estimation. An acrylic plate is installed above the thruster to mirror the boundary conditions of the Al_2O_3 plate below the thruster.

In order to quantify the velocity field using PIV, laser light from a Quantel EverGreen Nd:YAG

laser (Wavelength 532 nm) is directed through an articulated mirror arm and cylindrical optics to illuminate the plane of symmetry at mid-span of the emitter-collector pair. Due to the shadow cast by the collector, the region below it is invisible to the PIV. A pco.edge 5.5 sCMOS camera (resolution of 2560 x 2160 pixels, with a 16-bit depth) is installed slightly above the span-wise axis to reduce obstructions. This perspective distortion is corrected using a calibration target. The resulting scaling is $\sim 26\,\mathrm{pixel\,mm^{-1}}$, and double images are captured at a rate of 10 Hz and a pulse delay of 100 µs. The flow field is seeded with incense particles as these are generally regarded to be unaffected by the electric field [13, 16]. An enclosure of $1\,\mathrm{m} \times 1\,\mathrm{m} \times 1.5\,\mathrm{m}$ enables homogeneous tracer density.

Due to diffuse light reflection, and thus low signal-to-noise ratio in the vicinity of the collector, image preprocessing is performed. Average images are calculated and subtracted from the instantaneous images. Furthermore, the images are high-pass filtered with a 7 pixel kernel. The collector and accompanying shadow are masked. Multi-grid interrogation is used with an initial / final window size of 64 pixel / 8 pixel and an overlap of 50 %. For outlier detection, a normalized median test [17] with a threshold of 3.0, a maximum displacement test of 17 pixel, and a maximum displacement difference of 2 pixel are used. Outliers are replaced using lower-order peaks and interpolation.

2.2. Lagrangian Particle Tracking

Three-dimensional Lagrangian particle tracking (LPT) [18] by means of a 4-pulse shake-the-box (STB) system [19] is introduced to extend the flow diagnostics by valuable Lagrangian characteristics. Firstly, the data allows cross-validation of the two-dimensional assumption at the core of the PIV evaluations. Secondly, the material acceleration information along the Lagrangian particle tracks can directly be used to quantify the volumetric distribution of the ionic force.

Two different thruster configurations are investigated using STB. First is a wire-to-airfoil array configuration (W2A), as can be seen in Figure 3 and 4. Second is a wire-to-grid configuration (W2G) as shown in Figure 5 and Figure 6. Both configurations are adapted from the hybrid configurations of Usuelli et al. [15], and from Raffaello et al. [9], respectively. The W2A configuration retains all of the geometric parameters introduced in the PIV investigation with two distinct spacings for additional emitters S_e and collectors S_c.

The 4-pulse STB is comprised of two Quantel EverGreen Nd:YAG lasers, which are superimposed with a beam combiner to enable bursts of four consecutive pulses. Four LaVision Imager CX12 cameras (4080 x 2984 pixels, with a 12-bit depth) equipped with Scheimpflug adapters and 100 mm lenses (Milvus 2/100M, Zeiss) to record the particle images of the incense smoke from either side of a thick light sheet (indicated with green dashes in Figure 4). These lasers were fired in a $2:1:4$ ratio of time steps. The first two particle images were recorded on frame 1 of the cameras and the second two were recorded on frame 2. For all STB measurements 2000 frame pairs were

recorded at a repetition rate of 15 Hz.

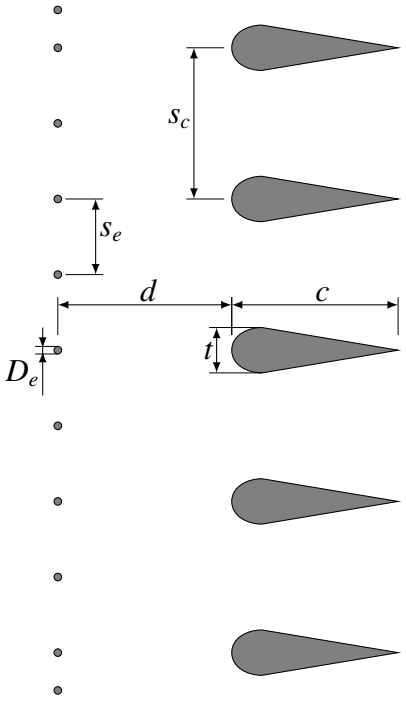


Figure 3. Array of wire-to-airfoil thrusters (W2A) in hybrid emitter configuration. Gap distance $d = 30$ mm, emitter diameter $D_e = 100$ µm, airfoil thickness $t = 6$ mm, airfoil chord $c = 25$ mm, collector spacing $s_c = 35$ mm, and emitter spacing $s_e = 17.5$ mm, with a spacing of the outermost emitters of $s_e = 7.5$ mm.

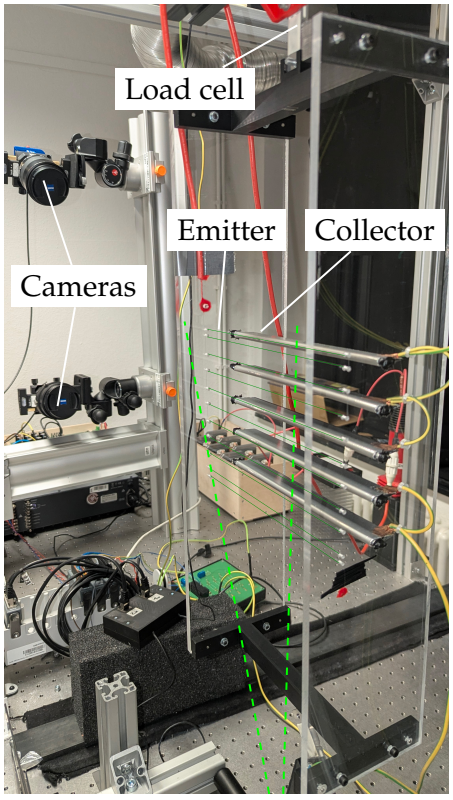


Figure 4. Experimental setup of the wire-to-airfoil array (W2A). Visibility of emitter wires is enhanced in dark green. Laser volume positioned at mid-span indicated by bright green dashed lines. Two of four cameras outside of frame, approximately mirrored with slight offset.

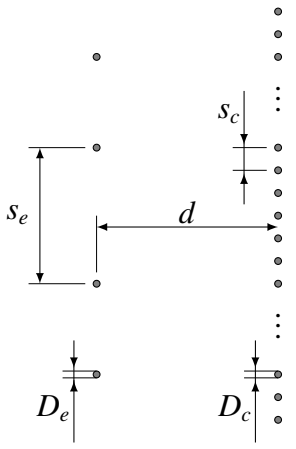


Figure 5. Thruster in wire-to-grid configuration (W2G). Gap distance $d = 20\,\text{mm}$, emitter diameter $D_e = 100\,\mu\text{m}$, collector diameter $D_c = 100\,\mu\text{m}$, collector spacing $s_c = 2.5\,\text{mm}$, and emitter spacing $s_e = 17.5\,\text{mm}$. Thruster frontal area is $200\,\text{mm} \times 200\,\text{mm}$, equating to 11 emitter wires.

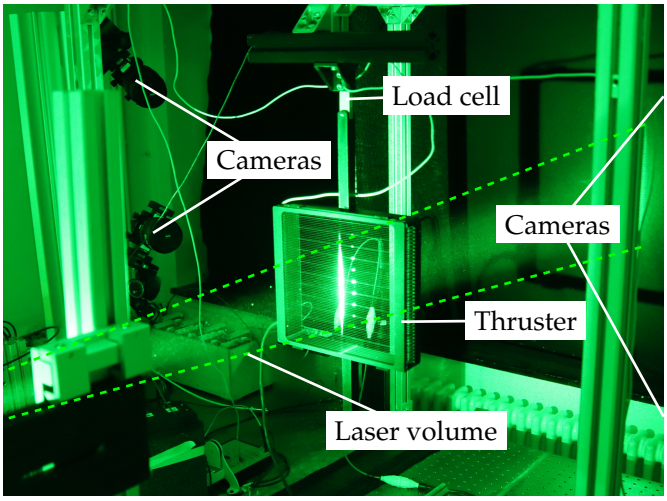


Figure 6. Experimental setup of the STB acquisition with the wire-to-grid (W2G) thruster. Emitting electrodes behind collecting electrodes from image point of view. Two of four cameras outside of frame, approximately mirrored with slight offset.

Due to the nature of the array hindering optical access for both laser light and cameras, the measurement volume is limited to upstream of the collectors' leading edge plane in the case of the W2A configuration. Recent Mach-Zehnder interferometry results by Poeppe et al. [20] revealed a significant change in air density between emitter and collector, as can be seen in Figure 7, which is considered to correlate with ion density and thus force distribution. As such, the choice of the restricted region of interest (ROI) nonetheless provides full optical access to the momentum-transfer domain between ions and neutrals for the desired force-field quantification.

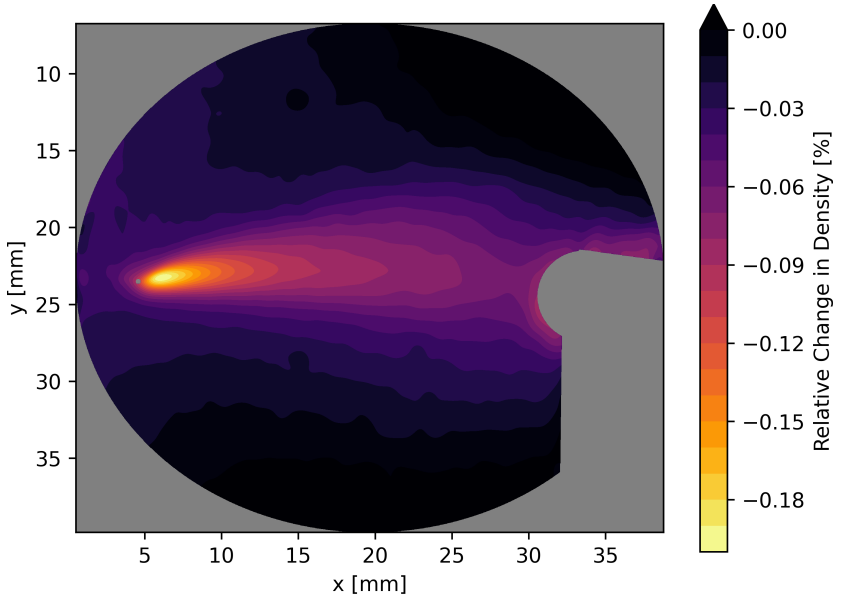


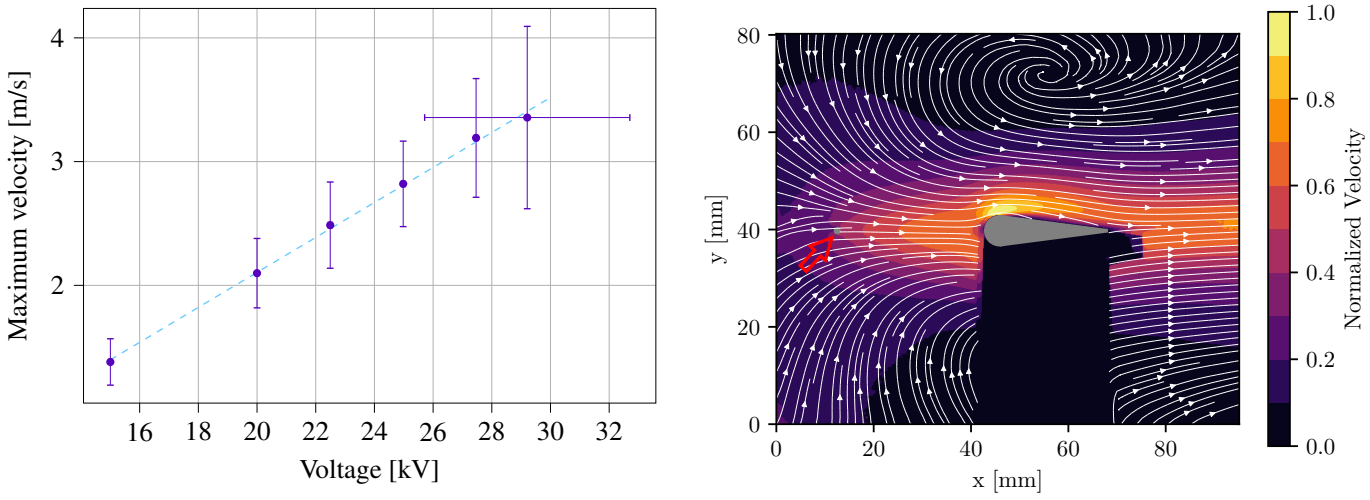
Figure 7. Relative change in air density in the drift region of an EAD thruster. Emitter is at $x \approx 5\,\text{mm}$, $y \approx 27\,\text{mm}$. Collector and collector frame are visible at the right edge of the field of view (Poeppe et al. [20]).

3. Evaluation of PIV Velocity Fields

This section addresses the discussion of flow fields and corresponding topology, while section 4 centers around the determination of momentum transfer and thrust from the velocity information.

3.1. Time-Averaged Velocity Fields

Since the velocity fields show strong topological similarity, and a linear relationship between voltage and velocity across the voltage range tested, this enables normalization and averaging across the voltage range. Such linear trends between operating voltage and velocity have also previously been reported by, e.g., Robinson [21]. The velocity fields are therefore normalized using their respective maximum velocities and averaged. Figure 8b shows the resulting normalized velocity field across all 6 voltages.



(a) Linear relationship between maximum velocity of the time-averaged velocity field and operating voltage.

(b) Normalized velocity field across all measured voltages. Emitter wire highlighted with red arrow. Emitter and collector in gray.

Figure 8. Normalization of six time-averaged velocity fields.

The normalized velocity field shows good agreement with numerical data generated by Picella et al. [22]. This holds true for all other evaluated velocity fields not shown here. A distinct flow acceleration region due to the body force of the corona-discharge momentum transfer can be seen between emitter and collector. A second acceleration region can be observed due to the suction peak of the collector airfoil shape. This leads to the maximum velocity coinciding with the location of maximum thickness.

Prominent vortices can be seen either above or below the thruster, possibly due to the presence of the acrylic and Al_2O_3 plates. However, these vortices only play a minor role in the momentum transfer, since they are entirely at near-zero velocities. Furthermore, the expected array configura-

tions of practical thruster designs will greatly influence the boundary conditions above and below a single emitter-collector pair and accordingly alter the global topology.

3.2. Instantaneous Velocity Fields

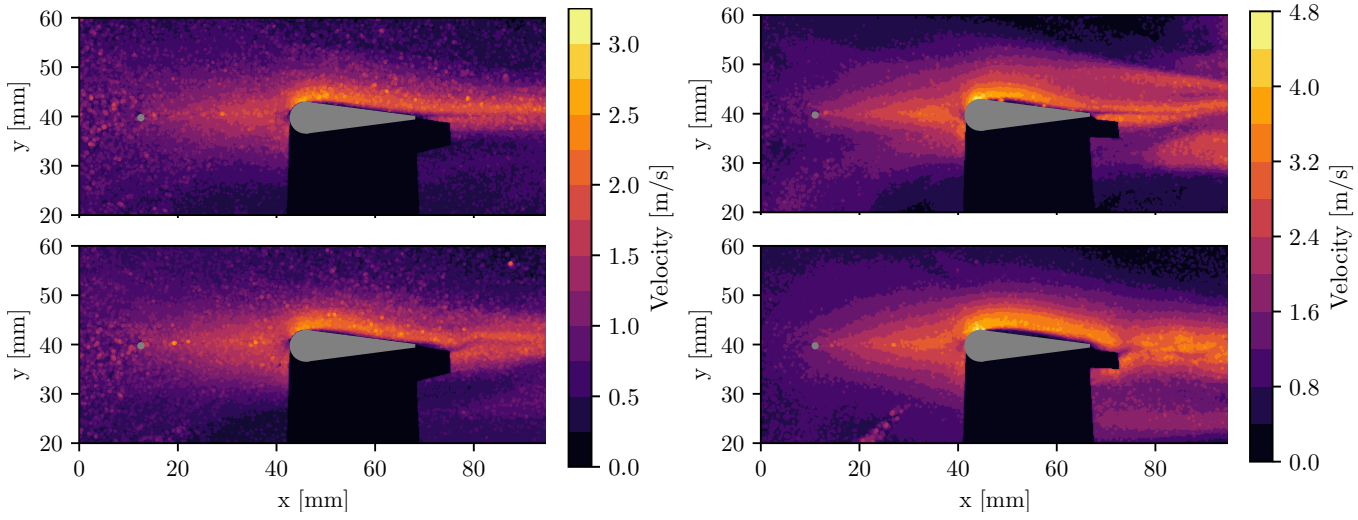
While the time-averaged velocity fields shown in subsection 3.1 appear to show a smooth and attached flow topology, the instantaneous velocity fields reveal the full picture of the largely unsteady flow character. Figure 9 contrasts two snapshots at 20 kV and 30 kV. While the top row shows a relatively smooth wake topology, the bottom row shows the onset of wake instabilities. Wake vortices in EAD thrusters are known and expected to occur in wire-to-cylinder configurations [13]; however, the present findings provide evidence that this vortex shedding can also occur with droplet airfoils. This insight is of particular importance to designs of multi-stage thruster arrays, since fluctuating inflow conditions at the downstream thrusters could lead to further increased instability and increases in aerodynamic losses.

The observed vortex formation could be due to an adverse pressure gradient at the suction peak, exacerbated by the non-uniform ionic-wind velocity distribution. An alternative explanation can be found in the sensitive behavior to small perturbations of the electric field of a single emitter-collector pair. In our experiments, the footprint of this could be seen in the streamlines of instantaneous velocity fields fluctuating up and down, even with laminar inflowing air. These results confirm earlier reports that emitter arrays are less susceptible to these velocity field fluctuations [23], which can be now explained on the grounds of velocity fields. While exhibiting other experimental difficulties, this insight immediately motivates the rigorous investigation of arrays with laser-optical field techniques. Of interest could be also a comparison of droplet airfoils to symmetric NACA airfoils with less severe adverse pressure gradient.

4. Velocity-Information-Based Thrust Estimation

As mentioned in subsection 2.1, the upstream rectifier is removed for this section. To assess the impact of this, a convergence analysis is conducted at the highest velocity in the flow field for both configurations (with and without rectifier), but otherwise unchanged setup and a constant operating voltage. Figure 10 shows the coefficient of variation, which is defined as σ/μ, with the standard deviation σ and the mean μ, each evaluated for the cumulative set of velocity fields $[1, 500]$. Even though the absence of the flow straightener obviously delays convergence, both configurations converge to a similar level, indicating a similar magnitude of velocity fluctuation. The figure shows the convergence analysis for 25 kV. Other voltages behave similarly.

Thrust is estimated using the integral momentum balance for a control volume (CV) of volume V



(a) 20kV (b) 30kV

Figure 9. Instantaneous velocity fields at random time stamps for 20 kV and 30 kV.

and surface area A as defined in Figure 2. The Integral momentum equation is given as

$$\frac{\mathrm{d}}{\mathrm{d}t}\iiint_V \rho u_j \,\mathrm{d}V + \iint_A \rho u_j u_i n_i \,\mathrm{d}A = -\iint_A p n_j \,\mathrm{d}A + \iint_A \tau_{ij} n_i \,\mathrm{d}A + \iiint_V \rho k_j \,\mathrm{d}V\,, \tag{1}$$

where ρ is the air density, u_j the velocity component in j-direction, n_i the normal vector of the CV boundary in i-direction, p the pressure, τ_{ij} the viscous shear stresses, and k_j are body forces.

For the present case of horizontal thrust, $j = 1$. Furthermore, steady flow is assumed and thus no temporal change of momentum is considered inside the CV. Viscous forces only exist on the top and bottom CV boundaries and on the collector surface A_c. At the top and bottom CV boundaries, they can be neglected at a sufficient distance. The inflowing and outflowing boundaries are similarly positioned at sufficient distance such that ambient pressure can be assumed and quiescent inflow conditions.

In the present case, the electroaerodynamic force F_{EAD} is the only non-negligible body force. Thus,

$$\iiint_V \rho k_1 \,\mathrm{d}V = \iiint_V \rho_q E \,\mathrm{d}V = F_{\mathrm{EAD}}\,, \tag{2}$$

where ρ_q is the space-charge density and E the electric field. Importantly, the electroaerodynamic force F_{EAD} must not be mistaken with the thrust T measured by the load cell, but rather the thrust T is equal to the electroaerodynamic body force F_{EAD} minus an unknown self-induced drag [24, 25] according to

$$T = F_{\mathrm{EAD}} - F_d\,, \tag{3}$$

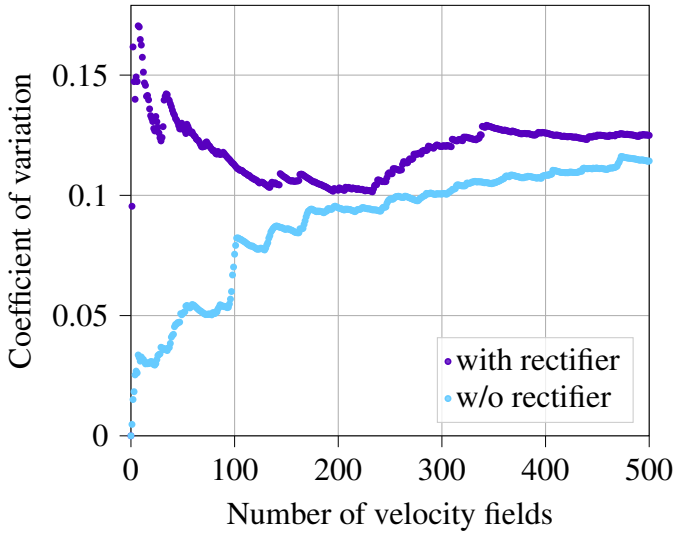


Figure 10. Convergence analysis of the location of maximum velocity for a voltage of 25 kV with and without rectifier. The measurement without rectifier extends to 1000 velocity fields but is cut off for comparability.

which is comprised of pressure and/or friction drag at emitter, collector, and other surfaces. The self-induced drag force F_d is dominated by the collector due to its size and is thus equal to the integral of the pressure and shear stress acting on the CV boundary A_c (see Figure 2), i.e.,

$$-\iint_{A_c} p n_1 \, \mathrm{d}A + \iint_{A_c} \tau_{i1} n_i \, \mathrm{d}A = -F_d \,, \tag{4}$$

whereby the relative contribution of pressure and friction drag to total drag remains unknown. Using the above assumptions, the 2D case can be simplified to

$$\int_{-\infty}^{\infty} \rho u_1^2 \, \mathrm{d}y = \frac{T}{b} \,, \tag{5}$$

where b is the span. Note that the integration bound of infinity is only valid for the case of quiescent environment. The formulation according to Equation 5 is similar to the one made by Hoskinson et al. [26] for use with dielectric barrier discharge (DBD) actuators in quiescent conditions.

Two notable investigations are presented in contrast to this approach. First, Belan et al. [27] used pitot measurements in an enclosed setup with a screen to reduce turbulence of the inflowing air. They positioned the inflowing boundary much closer to the thruster and did not neglect pressure p at the inflowing boundary and instead calculated the pressure losses due to the screen using Bernoulli's theorem.

Secondly, Monrolin et al. [13] do not neglect the inflowing momentum but do assume ambient pressure on all boundaries. By adding contributions of momentum fluctuations, they find a good agreement with their digital scale measurements.

Similarly, in the present study it has been found that fluctuations need to be taken into account in the momentum flux determination. This has been achieved by evaluating Equation 5 for each instantaneous velocity field and time-averaging the thrust. As can be seen in Figure 11, calculating the outflowing momentum flux from the average velocity field, thus discarding fluctuation contributions, leads to an underestimating of the resulting thrust estimate. additional consideration of the fluctuation contributions, significantly improves the agreement with the load cell measurement. The figure also makes apparent a drawback of estimating thrust from velocity data, where the advantage of a clear cause-effect relation between flow field and thrust resulting thrust estimate comes at the price of larger standard deviation compared to the load cell measurements.

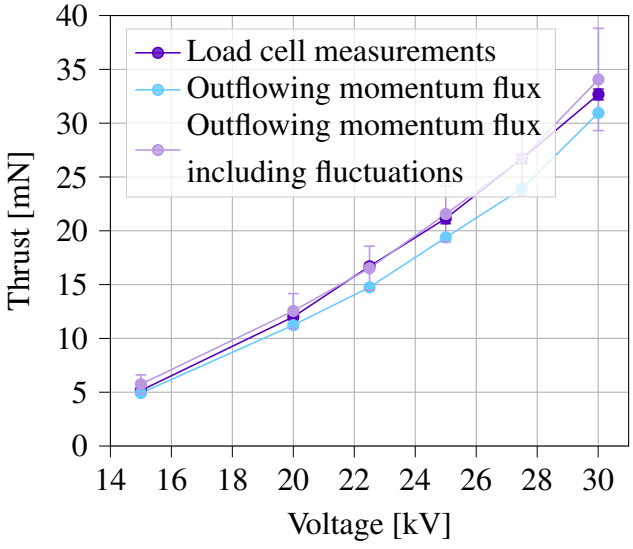


Figure 11. Two different methods of computing thrust from the momentum flux of measured velocity fields in comparison to direct load cell measurements.

5. Ionic Force Distribution

In contrast to earlier PIV-based efforts to determine body-force distributions resulting from gas discharges [28–30] by means of either the Navier-Stokes or the vorticity equations (NSE, VE), the major advantage of the Lagrangian data treatment centers around the fact that the determined accelerations along the recorded particle track immediately determine the material acceleration Du_i/Dt of the corresponding fluid elements. As such, the left-hand side of the NSE is immediately known from the experimental data, without separate determination of local and moreover convective accelerations from sparse data, since

$$a_j = \frac{Du_j}{Dt} = \frac{\partial u_j}{\partial t} + u_i \frac{\partial u_j}{\partial x_i}. \tag{6}$$

and the left-hand side of the NSE,

$$\frac{\mathrm{D}u_j}{\mathrm{D}t} = -\frac{1}{\rho}\frac{\partial p}{\partial x_j} + \nu\frac{\partial^2 u_j}{\partial x_i \partial x_i} + \frac{f_{j,\mathrm{EAD}}}{\rho} \tag{7}$$

is directly measured.

To improve the statistical significance of the obtained velocity u_j and acceleration a_j data, and the corresponding robustness of the fluid mechanical interpretation, an averaged version of Equation 7 is beneficial, which relies on the Reynolds decomposition.

Note that Equation 7 holds likewise true for the temporally averaged flow and acceleration fields, since the non-linear cross-correlation term of any occurring fluctuations (resulting from the Reynolds decomposition) appears first alongside the convective term, i.e.

$$\overline{\frac{\mathrm{D}u_j}{\mathrm{D}t}} = \frac{\partial \overline{u_j}}{\partial t} + \overline{u_i}\frac{\partial \overline{u_j}}{\partial x_i} + \overline{u_i'\frac{\partial u_j'}{\partial x_i}}\,, \tag{8}$$

and is then typically moved to all other forces on the right-hand side of the equation.

The so-called Reynolds-averaged Navier-Stokes (RANS) equations can accordingly be written as

$$\overline{a_j} = \overline{\frac{\mathrm{D}u_j}{\mathrm{D}t}} = -\frac{1}{\rho}\frac{\partial \overline{p}}{\partial x_j} + \nu\frac{\partial^2 \overline{u_j}}{\partial x_i \partial x_i} + \overline{\frac{f_{j,\mathrm{EAD}}}{\rho}}\,, \tag{9}$$

For the case of a W2G thruster, it is assumed that the viscous term is negligible. The validity of this will be shown in the results section. Monrolin et al. [13] note, that the pressure term cannot be directly determined and argue that the decomposition between pressure and volumetric force is of theoretical nature and experimentally irrelevant. While true, we expressly want to consider this distinction. Spatial integration of the fields leads to the above-mentioned decomposition into EAD body force F_{EAD}, self-induced drag F_d, and produced thrust T, which is based on similar approaches with surface-mounted DBD actuators. However, in the case of DBDs, the viscous term is non-negligible due to the interaction with the wall and the pressure term is negligible [26, 28–30]. For W2G thrusters we arrive at:

$$\iiint_V \overline{a_j}\,\mathrm{d}V = \frac{1}{\rho}\iiint_V \left(\overline{f_{j,\mathrm{EAD}}} - \frac{\partial \overline{p}}{\partial x_j}\right)\mathrm{d}V = F_{\mathrm{EAD}} - F_d = T\,. \tag{10}$$

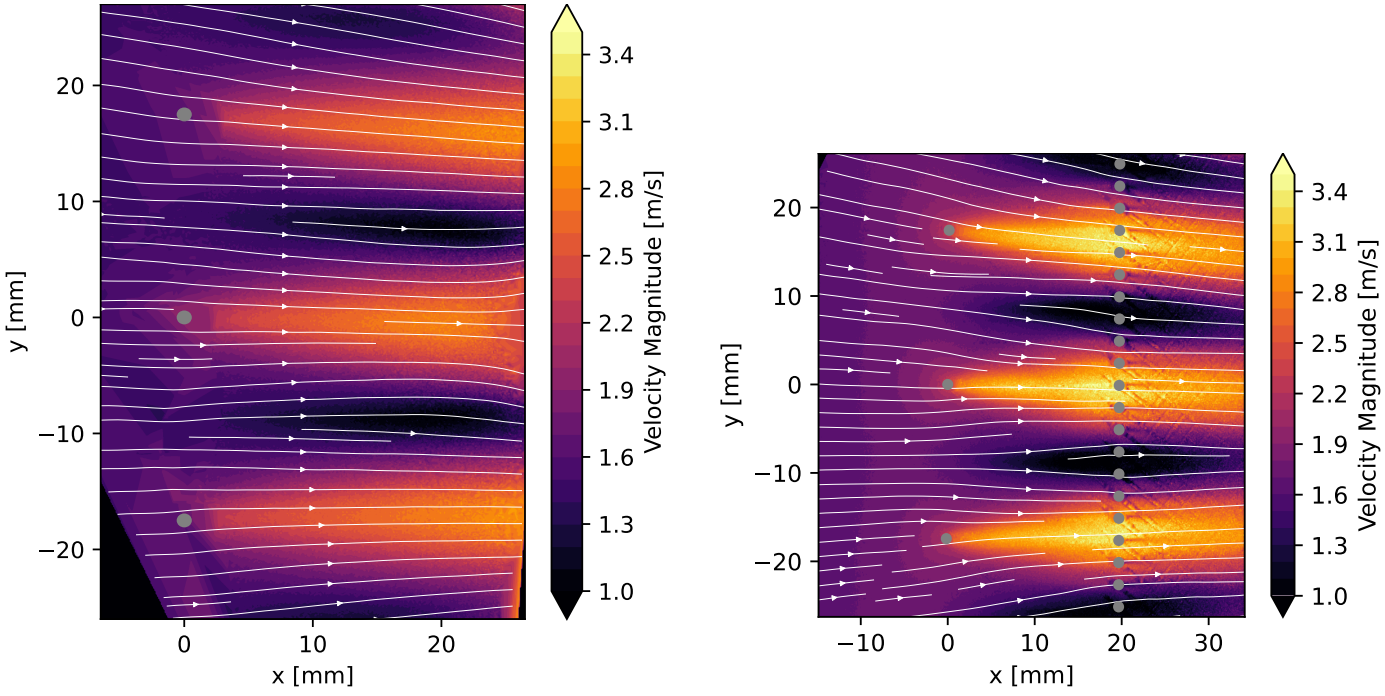
The same does not hold for W2A thrusters, since the viscous term cannot be ignored at the significant surface of the airfoil collectors.

Note that the density has been identified in subsection 2.2 to be quasi constant – at least for continuum mechanic considerations – such that ρ = const. is assumed in Equation 10.

Pasch et al. [31] already took advantage of this Lagrangian perspective for defocus particle tracking velocimetry (DPTV) data in context of barrier-discharge analysis and demonstrated a good approximation of the discharge-based body force by means of the recorded material accelerations.

6. Evaluation of LPT Velocity and Acceleration Fields

Figure 12 contrasts the velocity distribution of the two thruster configurations. Immediately visible is the much smaller field of view in Figure 12a due to optical access constraints and glare caused by the airfoil collectors and the emitter holes. Figure 12a nonetheless shows good agreement with the velocity field measured with PIV in subsection 3.1. Figure 12b clearly shows the locations of fast velocities between emitters and collector arrays. Furthermore, a wake can be spotted behind each collector wire, showcasing the sensitivity of W2G thrusters to the blockage ratio of the collector grid and its accompanying pressure drag. Closer inspection reveals diagonal measurement artifacts in the vicinity and to the right of the collectors, caused by obstruction of the line of sight of the cameras by the collector wires and especially their glare.



(a) W2A gap $d = 30\,\text{mm}$, operating voltage $V = 30\,\text{kV}$.

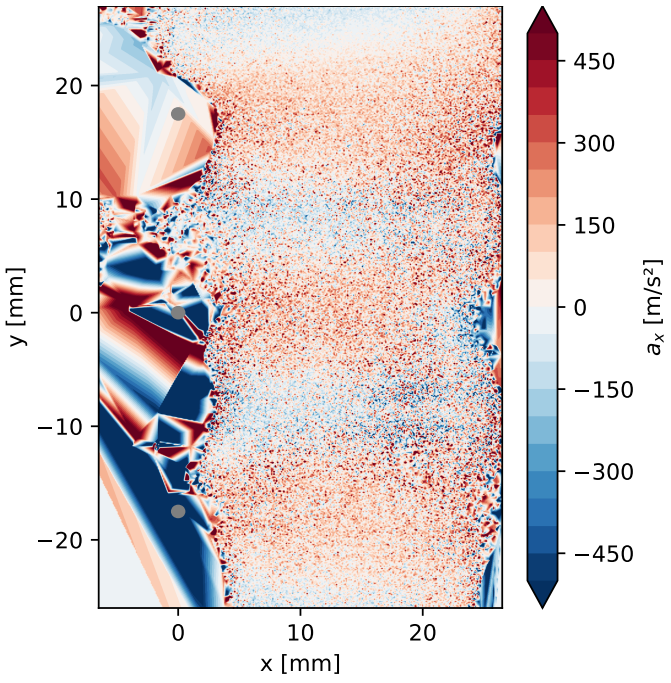
(b) W2G distance $d = 20\,\text{mm}$, operating voltage $V = 20\,\text{kV}$.

Figure 12. Experimental LPT results: Velocity magnitude for the two different thruster configurations. Emitters and grid wires are indicated in gray (not to scale).

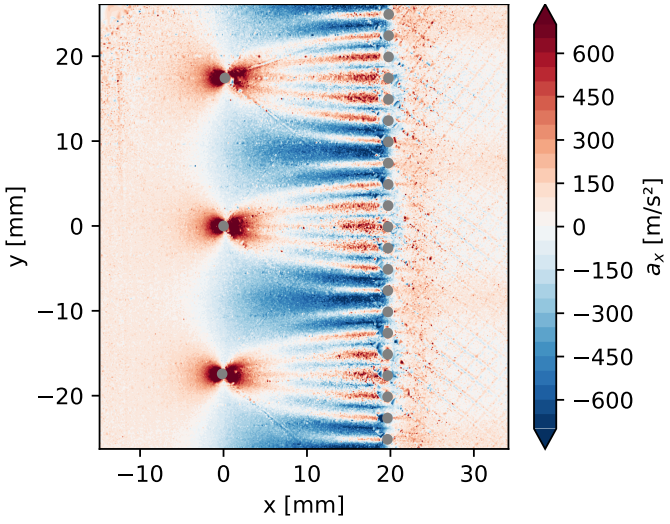
The corresponding acceleration fields are shown in Figure 13. In Figure 13a the above-mentioned optical issues become even more apparent, exacerbated by the fact that fewer particle tracks were successfully recovered, presumably due to slight distortion of the acrylic frame. Since we deem the quality of the results in Figure 13a inadequate for the time being, the rest of the evaluation will focus on the W2G thruster. Figure 13b reveals salient channels of acceleration from the emitters towards distinct collector wires. This is the first time such channels were observed experimentally and showcases the possibilities of STB LPT in this context.

There are a couple more notable observations to be made. First, there is a region of acceleration upstream of the emitters caused by a suction of the thrusters. Second, deceleration dominates in the drift region. Particles not in the acceleration channels experience a pressure drag caused by the collector wires. Third, downstream of the collectors, a slight acceleration region can once again be observed. This is presumably due to pressure equalization following the blockage of the collector grid.

Integrating the acceleration data over a sufficiently large volume would yield the net thrust and could be compared to the load cell measurements, similar to section 4. However, there are regions outside of the field of view with significant acceleration magnitudes that cannot be neglected. Thus this comparison is not possible with the available data.



(a) W2A gap $d = 30\,\text{mm}$, operating voltage $V = 30\,\text{kV}$. Data shows severe issues in the emitter region, relatively sparse data in the drift region and terminates before the collectors. Therefore, the rest of the analysis will focus on the W2G acceleration field.



(b) W2G distance $d = 20\,\text{mm}$, operating voltage $V = 20\,\text{kV}$.

Figure 13. Experimental LPT results: Streamwise component of material acceleration $a_x(x, y) = \mathrm{D}u_x(x, y)/\mathrm{D}t$ for the two different thruster configurations. Emitters and grid wires are indicated in gray (not to scale).

Figure 14 backs up the earlier assumption of the viscous term of the NSE being negligible, as it shows this term derived from the velocity information. The magnitude of the viscous term is negligible compared to the material acceleration.

Recall that the immediate measurement of the lefthand side of the RANS Equation 9, i.e. $\overline{\frac{\mathrm{D}u_j}{\mathrm{D}t}}$ in turn provides the righthand side of NSE without the typical issues stemming from Eulerian data

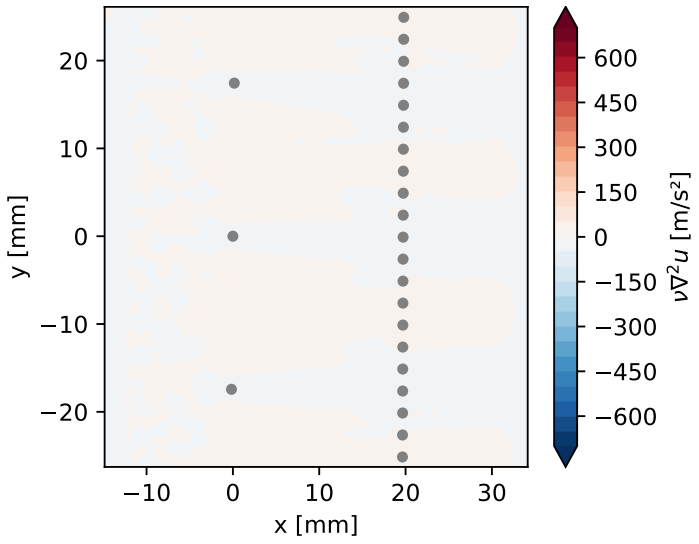


Figure 14. Viscous term derived from the velocity data (cp. Equation 9) for W2G distance $d = 20\,\text{mm}$ and operating voltage $V = 20\,\text{kV}$. Gaussian smoothing with 2 mm kernel size to eliminate numerical noise.

generation. As such, Figure 13 provides a picture of the sum of body forces, pressure gradients and viscous terms as occur for the given flow scenario and in the case of Figure 13b the sum of body force and pressure gradients only. Consequently, candidating locations of body force (BF) distributions can be spotted unless pressure gradients are present. To distinguish real BFs from pressure-driven contributors, the above-discussed density fields provide a first step, which we expect to expand further soon.

7. Conclusions

The present work showcases high-resolution near-wall velocity fields in the vicinity of an electroaerodynamic thruster. Time-averaged velocity fields show the operating-voltage-invariant flow field topology, while instantaneous flow fields reveal the presence of significant wake instabilities and vortex shedding. The performance and stability of multi-stage thruster arrays could be impacted by fluctuating inflow conditions created by upstream thrusters. Future investigations should investigate the impact of the collector shape on wake instabilities.

Accurate thrust estimation from particle image velocimetry data was shown in the quiescent case. Crucially, the integral momentum balance must account for momentum flux fluctuations, as the momentum flux of the time-averaged velocity field underestimates the thrust measured by the load cell. While the thrust estimation was accurate across a large range of voltages, a drawback remains in the much greater standard deviation when compared to the load cell measurements.

We can confidently claim that LPT velocimetry by means of 4-pulse STB has significant potential for investigating EAD thrusters and allows novel insight into the ionic force distribution and

could enable future momentum transfer improvements. Of particular interest is the channel-like distribution of the ionic force in W2G configurations which to our knowledge has not been identified before. LPT proves less useful for W2A configuration because optical access is hindered and large amounts of glare complicate the processing further. In contrast, for W2G configurations, it allows unparalleled insight into velocity and acceleration distributions, extending upstream and downstream of the thruster, where significant magnitudes of acceleration due to pressure gradients could be measured.

8. Acknowledgments

This project has received funding from the European Union's Horizon Europe Research and Innovation Programme under grant agreement No 101098900. Views and opinions expressed are however those of the author(s) only and do not necessarily reflect those of the European Union or European Innovation Council and SMEs Executive Agency (EISMEA). Neither the European Union nor the granting authority can be held responsible for them.

Furthermore, financial support by the Deutsche Forschungsgemeinschaft (DFG, German Research Foundation) through project number 513183059 and the Struktur- und Innovationsfonds Baden-Württemberg (SI-BW, structural and innovation funds of Baden-Wuerttemberg) for the laser-optical measurement equipment is gratefully acknowledged.

In addition, TR acknowledges support through the Alexander von Humboldt Foundation.

References

[1] Omar Kahol, Marco Belan, Mattia Pacchiani, and Domenico Montenero. Scaling relations for the geometry of wire-to-airfoil atmospheric ionic thrusters. *Journal of Electrostatics*, 123:103815, May 2023. doi: 10.1016/j.elstat.2023.103815.

[2] Nicolas Gomez-Vega, Haofeng Xu, James M. Abel, and Steven R. H. Barrett. Performance of decoupled electroaerodynamic thrusters. *Applied Physics Letters*, 118(7):074101, February 2021. doi: 10.1063/5.0038208.

[3] Jack Wilson, Hugh D. Perkins, and William K. Thompson. An Investigation of Ionic Wind Propulsion. *NASA Glenn Research Center*, (NASA/TM-2009-215822), December 2009.

[4] Eric Moreau, Nicolas Benard, Jean-Daniel Lan-Sun-Luk, and Jean-Pierre Chabriat. Electrohydrodynamic force produced by a wire-to-cylinder dc corona discharge in air at atmospheric pressure. *Journal of Physics D: Applied Physics*, 46(47):475204, October 2013. doi: 10.1088/0022-3727/46/47/475204.

[5] N. Monrolin, F. Plouraboué, and O. Praud. Electrohydrodynamic Thrust for In-Atmosphere Propulsion. *AIAA Journal*, 55(12):4296–4305, December 2017. doi: 10.2514/1.J055928.

[6] V. Yu. Khomich, V. E. Malanichev, and I. E. Rebrov. Electrohydrodynamic thruster for near-space applications. *Acta Astronautica*, 180:141–148, March 2021. doi: 10.1016/j.actaastro.2020.12.002.

[7] Haofeng Xu, Yiou He, Kieran L. Strobel, Christopher K. Gilmore, Sean P. Kelley, Cooper C. Hennick, Thomas Sebastian, Mark R. Woolston, David J. Perreault, and Steven R. H. Barrett. Flight of an aeroplane with solid-state propulsion. *Nature*, 563(7732):532–535, November 2018. doi: 10.1038/s41586-018-0707-9.

[8] Marco Belan, Raffaello Terenzi, Stefano Trovato, and Davide Usuelli. Effects of the emitters density on the performance of an atmospheric ionic thruster. *Journal of Electrostatics*, 120: 103767, November 2022. doi: 10.1016/j.elstat.2022.103767.

[9] Terenzi Raffaello, Trovato Stefano, Usuelli Davide, and Belan Marco. Atmospheric electroaerodynamic thrusters with grid collectors. *Scientific Reports*, 15(1):41513, November 2025. ISSN 2045-2322. doi: 10.1038/s41598-025-25308-6. Publisher: Nature Publishing Group.

[10] Kento Masuyama and Steven R. H. Barrett. On the performance of electrohydrodynamic propulsion. *Proceedings of the Royal Society A: Mathematical, Physical and Engineering Sciences*, 469(2154):20120623, June 2013. doi: 10.1098/rspa.2012.0623.

[11] C. Luke Nelson and Daniel S. Drew. High Aspect Ratio Multi-Stage Ducted Electroaerodynamic Thrusters for Micro Air Vehicle Propulsion. *IEEE Robotics and Automation Letters*, 9(3): 2702–2709, March 2024. ISSN 2377-3766. doi: 10.1109/LRA.2024.3355728.

[12] Nicolas Gomez-Vega and Steven R. H. Barrett. Order-of-Magnitude Improvement in Electroaerodynamic Thrust Density with Multistaged Ducted Thrusters. *AIAA Journal*, 62(4):1342–1353, April 2024. ISSN 0001-1452. doi: 10.2514/1.J063431. URL https://arc.aiaa.org/doi/10.2514/1.J063431.

[13] Nicolas Monrolin, Olivier Praud, and Franck Plouraboué. Electrohydrodynamic ionic wind, force field, and ionic mobility in a positive dc wire-to-cylinders corona discharge in air. *Physical Review Fluids*, 3(6):063701, June 2018. ISSN 2469-990X. doi: 10.1103/PhysRevFluids.3.063701. URL https://link.aps.org/doi/10.1103/PhysRevFluids.3.063701.

[14] Stefano Trovato, Raffaello Terenzi, Davide Usuelli, and Marco Belan. Wind tunnel testing and performance modeling of an atmospheric ion thruster. *Journal of Physics D: Applied Physics*, 58(1):015201, October 2024. ISSN 0022-3727. doi: 10.1088/1361-6463/ad7d9c. URL https://dx.doi.org/10.1088/1361-6463/ad7d9c. Publisher: IOP Publishing.

[15] Davide Usuelli, Raffaello Terenzi, Stefano Trovato, and Marco Belan. Performance Enhancement of EAD Thrusters With Nonuniform Emitters Array. *IEEE Transactions on Plasma Science*, 52(11):5414–5421, November 2024. ISSN 1939-9375. doi: 10.1109/TPS.2024.3505980. URL https://ieeexplore.ieee.org/document/10785549.

[16] M. Hamdi, M. Havet, O. Rouaud, and D. Tarlet. Comparison of different tracers for PIV measurements in EHD airflow. *Experiments in Fluids*, 55(4):1702, March 2014. ISSN 1432-1114. doi: 10.1007/s00348-014-1702-z. URL https://doi.org/10.1007/s00348-014-1702-z.

[17] Jerry Westerweel and Fulvio Scarano. Universal outlier detection for PIV data. *Experiments in Fluids*, 39(6):1096–1100, December 2005. ISSN 1432-1114. doi: 10.1007/s00348-005-0016-6. URL https://doi.org/10.1007/s00348-005-0016-6.

[18] Andreas Schröder and Daniel Schanz. 3d lagrangian particle tracking in fluid mechanics. *Annual Review of Fluid Mechanics*, 55(Volume 55, 2023):511–540, 2023. ISSN 1545-4479. doi: https://doi.org/10.1146/annurev-fluid-031822-041721. URL https://www.annualreviews.org/content/journals/10.1146/annurev-fluid-031822-041721.

[19] Matteo Novara, Daniel Schanz, Nico Reuther, Christian J. Kähler, and Andreas Schröder. Lagrangian 3d particle tracking in high-speed flows: Shake-the-box for multi-pulse systems. *Experiments in Fluids*, 57, 8 2016. ISSN 07234864. doi: 10.1007/s00348-016-2216-7.

[20] Dominic Poeppe, Alina Kuhn, and Jochen Kriegseis. Velocity and Density Characterization around Ionic Thrusters in Wire-to-Airfoil Configuration. 2025. URL https://publikationen.bibliothek.kit.edu/1000186731.

[21] Myron Robinson. Movement of air in the electric wind of the corona discharge. *Transactions of the American Institute of Electrical Engineers, Part I: Communication and Electronics*, 80(2):143–150, May 1961. ISSN 2379-674X. doi: 10.1109/TCE.1961.6373091. URL https://ieeexplore.ieee.org/document/6373091.

[22] Francesco Picella, David Fabre, and Franck Plouraboué. Numerical Simulations of Ionic Wind Induced by Positive DC-Corona Discharges. *AIAA Journal*, 62(7):2562–2573, July 2024. ISSN 0001-1452. doi: 10.2514/1.J063325. URL https://arc.aiaa.org/doi/10.2514/1.J063325. Publisher: American Institute of Aeronautics and Astronautics.

[23] M Belan, J Baldo, O Kahol, and D Montenero. Blade emitters for atmospheric ionic thrusters. *Journal of Physics D: Applied Physics*, 57(19):195201, February 2024. ISSN 0022-3727. doi: 10.1088/1361-6463/ad266a. URL https://dx.doi.org/10.1088/1361-6463/ad266a.

[24] C. Enloe, M. McHarg, Gabriel Font, and Thomas McLaughlin. Plasma-induced Force and Self-induced Drag in the Dielectric Barrier Discharge Aerodynamic Plasma Actuator. In

47th AIAA Aerospace Sciences Meeting including The New Horizons Forum and Aerospace Exposition, Aerospace Sciences Meetings. American Institute of Aeronautics and Astronautics, January 2009. doi: 10.2514/6.2009-1622. URL https://arc.aiaa.org/doi/10.2514/6.2009-1622.

[25] J. Kriegseis, S. Grundmann, and C. Tropea. Power consumption, discharge capacitance and light emission as measures for thrust production of dielectric barrier discharge plasma actuators. *Journal of Applied Physics*, 110(1):013305, July 2011. ISSN 0021-8979. doi: 10.1063/1.3603030. URL https://doi.org/10.1063/1.3603030.

[26] A R Hoskinson, N Hershkowitz, and D E Ashpis. Force measurements of single and double barrier DBD plasma actuators in quiescent air. *Journal of Physics D: Applied Physics*, 41(24):245209, November 2008. ISSN 0022-3727. doi: 10.1088/0022-3727/41/24/245209. URL https://dx.doi.org/10.1088/0022-3727/41/24/245209.

[27] Marco Belan, Luca Arosti, Riccardo Polatti, Filippo Maggi, Samuele Fiorini, and Federico Sottovia. A parametric study of electrodes geometries for atmospheric electrohydrodynamic propulsion. *Journal of Electrostatics*, 113:103616, September 2021. ISSN 0304-3886. doi: 10.1016/j.elstat.2021.103616. URL https://www.sciencedirect.com/science/article/pii/S0304388621000632.

[28] M Kotsonis, S Ghaemi, L Veldhuis, and F Scarano. Measurement of the body force field of plasma actuators. *Journal of Physics D: Applied Physics*, 44(4):045204, jan 2011. doi: 10.1088/0022-3727/44/4/045204. URL https://doi.org/10.1088/0022-3727/44/4/045204.

[29] N Benard, A Debien, and E Moreau. Time-dependent volume force produced by a non-thermal plasma actuator from experimental velocity field. *Journal of Physics D: Applied Physics*, 46(24):245201, May 2013. ISSN 0022-3727. doi: 10.1088/0022-3727/46/24/245201. URL https://doi.org/10.1088/0022-3727/46/24/245201. Publisher: IOP Publishing.

[30] J. Kriegseis, C. Schwarz, C. Tropea, and S. Grundmann. Velocity-information-based force-term estimation of dielectric-barrier discharge plasma actuators. *Journal of Physics D: Applied Physics*, 46(5):055202, January 2013. ISSN 0022-3727. doi: 10.1088/0022-3727/46/5/055202. URL https://dx.doi.org/10.1088/0022-3727/46/5/055202. Publisher: IOP Publishing.

[31] Saskia Pasch, Heinrich L. Lange, Robin Leister, and Jochen Kriegseis. Defocusing PTV flow measurements above a DBD plasma actuator array for oscillatory forcing. *Experiments in Fluids*, 66(9):172, August 2025. ISSN 1432-1114. doi: 10.1007/s00348-025-04090-1. URL https://doi.org/10.1007/s00348-025-04090-1.